

4 The Role of Gas in Determining Image Quality and Resolution During In Situ Scanning Transmission Electron Microscopy Experiments

Yuanyuan Zhu*^[a] and Nigel D. Browning^[a, b]

As gas–solid heterogeneous catalytic reactions are molecular in nature, a full mechanistic understanding of the process requires atomic-scale characterization under realistic operating conditions. Although atomic resolution imaging has become routine in modern high-vacuum (scanning) transmission electron microscopy ((S)TEM), both image quality and resolution nominally degrade on introduction of the reaction gases. In this work, we systematically assess the effects of different gases at various pressures on the quality and resolution of

images obtained at room temperature in the annular dark field STEM imaging mode by using a differentially pumped (DP) gas cell. This imaging mode is largely free from inelastic scattering effects induced by the presence of gases and retains good imaging properties over a wide range of gas mass/pressures. We demonstrate the application of ESTEM with atomic resolution images for a complex oxide alkane oxidation catalyst MoVNbTeO_x (M1) immersed in light and heavy gas environments.

Introduction

Directly monitoring heterogeneous catalysts under catalytic conditions is key to obtaining insights into their behavior. Currently, environmental (scanning) transmission electron microscopy (E(S)TEM) is the only characterization tool that can provide atomic-site specific observations of local catalyst surface structure during solid–gas reactions.^[1] In this approach, a volume of pressurized gas is introduced and maintained tightly around a TEM sample through either a differential pumping mechanism (DP) or by a membrane windowed (MW) gas cell.^[2] The use of in situ TEM has progressed from pioneering early work featuring self-built modifications to existing microscopes/holders^[3] to the use of commercially manufactured^[4] instruments. However, the gaseous environment (and its container) continues to limit the (S)TEM sensitivity and resolvability in characterizing the solid catalyst owing to an increase in scattering events from the background gases/windows. To achieve better imaging sensitivity and resolvability in catalytically relevant gaseous environments, it is therefore crucial to under-

stand how the gas molecules affect the scattering of fast electrons contributing to the atomic-scale image.^[5]

There are two basic atomic imaging modes in (S)TEM, the conventional high-resolution transmission electron microscope (HR-TEM) phase contrast image and the incoherent annular dark-field scanning transmission electron microscopy (ADF-STEM) image. Although environmental HR-TEM (HR-ETEM mode) has been widely used for in situ observations of heterogeneous catalysts and provides quantitative atomic information with the aid of image simulations,^[6] environmental ADF-STEM (ESTEM mode) has already started demonstrating promising advantages for imaging supported metallic nanocatalysts^[7] with single-atom sensitivity,^[8] and for offering directly interpretable images of atomic-scale dynamics in complex oxide catalysts.^[9] Additionally, analytical techniques including energy-dispersive X-ray spectroscopy (EDX) and electron energy loss spectroscopy (EELS) in ADF-STEM mode (i.e., STEM-EDS and STEM-EELS) can also provide localized compositional and electronic information.^[7b,10] Despite these potential advantages of ESTEM, the effect of the gas environment on the image quality has so far only been discussed for the HR-ETEM imaging mode.^[5a,11]

In this work, we conduct the first experimental evaluation of the quality and resolution of the DP-ESTEM imaging mode (in a non-aberration-corrected STEM) under the influence of various gas environments at different pressures. One of the main constraints of DP-ESTEM is the lower DP aperture, which limits the ADF detector outer acceptance angle. We examine this issue by using a uniform solid sample—the standard lacy amorphous carbon, whose low atomic weight (*Z*) renders it as a touchstone for evaluating the gas effects on ESTEM contrast and on image signal-to-noise ratio (SNR), with different ADF collection ranges. As catalysts and particularly their atomic de-

[a] Dr. Y. Zhu, Prof. Dr. N. D. Browning
Physical & Computational Science Directorate
Pacific Northwest National Laboratory
Richland, WA 99352 (USA)
E-mail: yuanyuanzhu2014@gmail.com
nigel.browning@pnnl.gov

[b] Prof. Dr. N. D. Browning
Department of Materials Science and Engineering
University of Washington
Seattle, WA 98195 (USA)

Supporting information and the ORCID identification number(s) for the author(s) of this article can be found under <https://doi.org/10.1002/cctc.201700474>.

This publication is part of a Special Issue on “Advanced Microscopy and Spectroscopy for Catalysis”.

tails in gas environments are usually the main interest of in situ microscopy observations, we also show how the gases affect the ESTEM SNR and resolution in atomic resolution images of crystalline MoVnBTeO_x (M1) catalysts. All evaluations were conducted at room temperature, for high temperature imaging also depends on the stability of the heating stage used, which is beyond the scope of this study.

Results and Discussion

Effect of gas on ESTEM image quality for amorphous carbon (i.e., at low spatial resolution)

Figure 1 a–d shows experimental DP-ESTEM images of regions with and without the solid carbon sample, in four commonly used gases at pressures from high vacuum (2×10^{-7} mbar) to 10 mbar.

Considering that the DP gas cell apertures (especially the ones below the sample) confine the scattering angle of exit electrons and impose a 71 mrad cut-off, we choose an ADF detector inner semi-angle of approximately 21 mrad to provide an adequate collection range of 21–71 mrad (i.e., a low-angle annular dark field (LAADF) with intensity $\sim Z^2$, α : 1.0–1.3^[12]). Notably, a low probe current of < 3 pA was used throughout this work to reflect the practical ESTEM conditions usually used for imaging beam-sensitive catalysts (for dose and dose-rate definitions see the Experimental Section). As shown in, for ex-

ample, the intensity line profiles of the pressure series in N_2 gas (Figure 1 e), the gas environment leads to an increasing intensity of the gas background (and of the solid sample as the gas is all around the sample); meanwhile, the noise level in the linescans also increases slightly along with N_2 pressure (section 1 in the Supporting Information).

More importantly, if the N_2 pressure series is normalized to the corresponding gas background intensity (I_{gas}), in Figure 1 f, the contrast of the carbon decreases as the pressure increases. We define the ESTEM contrast of the lacy carbon as the difference between the intensity of carbon and gas background versus the gas intensity (Weber contrast): $(I_{\text{carbon}} - I_{\text{gas}}) / I_{\text{gas}}$. This ESTEM carbon contrast, if normalized to the initial contrast in the vacuum (Figure 1 g) decreases by about 55% in N_2 and Ar at 10 mbar. The “useful signal” from a sample degrades as the gas pressure/mass increases. To examine to what extent the presence of gases influences the “image signal of a sample”, here, we define the signal/noise ratio (SNR) as the intensity from the carbon $(I_{\text{carbon}} - I_{\text{gas}})$ divided by the standard deviation of the sample raw counts ΔI_{carbon} . Thus, the higher the SNR (the values in Figure 1 h at low gas pressures), the better the imaging ability to observe the structural and chemical features of a sample. In contrast, as the gas pressure/mass increases the net carbon intensity starts to become comparable with its noise level, inducing uncertainties in the observation of the solid sample. The SNR is found to be more strongly confined by the gas environment if the ESTEM images are collected

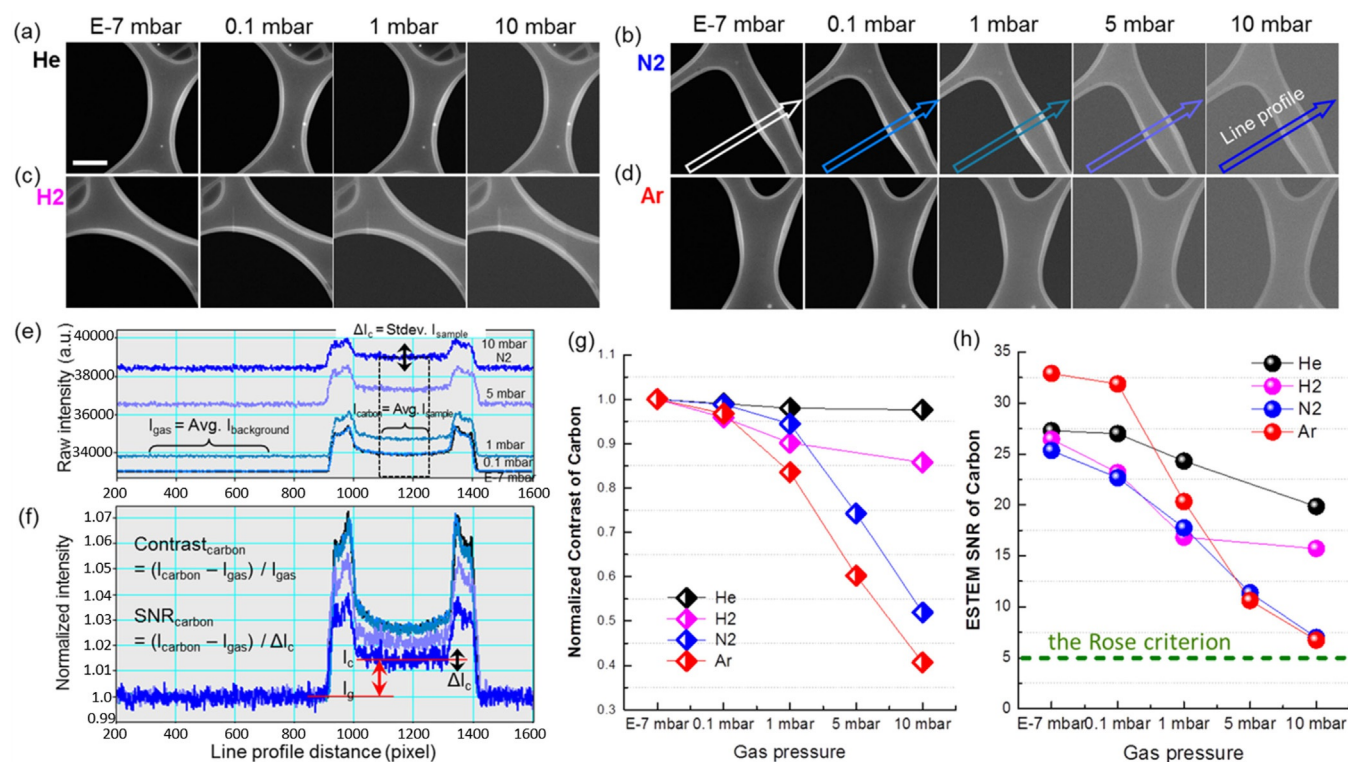


Figure 1. Experimental ESTEM images of gas background and amorphous lacy carbon from high vacuum to 10 mbar in a) He, b) N_2 , c) H_2 , and d) Ar. All images are under the same magnification, and the scale bar is 200 nm. e) Intensity line profiles in raw counts from gas background to the carbon sample in N_2 at different pressures. The measurement of I_{gas} , I_{carbon} , and ΔI_{carbon} are defined. f) Normalized experimental carbon intensity to corresponding I_{gas} , showing the carbon contrast change against the N_2 background at different pressures. The calculations of $\text{Contrast}_{\text{carbon}}$ and $\text{SNR}_{\text{carbon}}$ are defined. g) Normalized experimental ESTEM $\text{Contrast}_{\text{carbon}}$ ($(I_{\text{carbon}} - I_{\text{gas}}) / I_{\text{gas}}$) and h) $\text{SNR}_{\text{carbon}}$ in He, H_2 , N_2 , and Ar gas environments as a function of pressure. The Rose criterion ($\text{SNR} > 5$) is marked to show the preserved high SNR of carbon in heavy gas up to 10 mbar.

under a medium-angle annular (MAADF) setting (section 2 in the Supporting Information). However, for the LAADF mode with a relatively large collection range, the ESTEM SNR of the light carbon remains above the Rose criterion^[13] in 10 mbar Ar. Thus, for a given catalytic sample (often a fixed Z-number) the inner ADF collection angle can be used to leverage heavy gas and high pressure environment with controlled electron dose/dose-rate in DP-ESTEM, without introducing contrast reversals (even for light carbon) while maintaining a good sample contrast and SNR.

Considering that the STEM ADF detector is an electron-counting device, the raw image intensity faithfully counts the forward scattered electrons collected by the detector. The observed increases in ESTEM intensity and more importantly in the noise level from the area of the carbon suggest that there are additional “unwanted” electrons scattered by the gas molecules onto the ADF detector. These “extra electrons” cause the changes in the intensity as well as in the noise level in environmental images. To quantitatively assess to what extent this gas-induced scattering affects the ETEM and ESTEM imaging modes, we calculated the cross sections of elastic and inelastic scattering by the gases under the two imaging settings (section 3 in the Supporting Information). As shown in Figure 2,

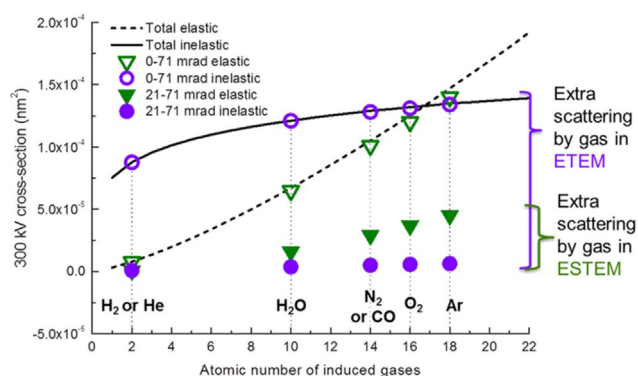


Figure 2. Theoretically calculated cross sections of elastically and inelastically scattered electrons at different scattering angular ranges as a function of the atomic number of the object the electrons (with an incident energy of 300 kV) interact with. Different types of gases are marked based on their atomic number. For a Titan DP environmental microscope, the scattered electrons collected in the ETEM imaging mode is 0–71 mrad (assume no objective aperture used), and an annular range of 21–71 mrad was collected by the LAADF-ESTEM imaging mode used in this work.

the ETEM imaging mode records almost all the extra inelastic noise from the gases at low scattering angles (open symbols); whereas the ESTEM mode excludes most of it (inelastic characteristic scattering angles of typical gases are <0.25 mrad in Table S1 in the Supporting Information). In the ESTEM mode, the relatively low total extra scattering (from the gas molecules) explains the high imaging sensitivity (i.e., SNR) in the sample. The advantage of the ADF-STEM mode in revealing catalytic nanoparticles on a thick support background^[14] also applies to imaging the materials in gases (the gas volume and the windows for MW gas cells are now the background of the signal).

Effect of gas on ESTEM atomic resolution image quality for the M1 catalyst

Next, we investigated the gas effect on the atomically resolved ESTEM images. Because of its large lattice parameter and good stability in a gas environment,^[9] the crystalline M1 catalyst was employed for this evaluation. Figure 3a,b presents high-resolution ESTEM pressure series of the M1 crystal in [001] projection in He and N₂ environments, respectively. To further quantify the gas effect, we performed a fast Fourier transform (FFT) based signal analysis, which is better suited for measuring atomically resolved lattice images. For example, Figure 3c shows the FFT-based SNR measurement on an M1 atomic ESTEM image (details of this method are given in the Experimental Section). The results show, in Figure 3d, the SNR_{M1} is, as expected, higher in the light He than that in the heavier N₂ at the same pressure. At 10 mbar, the ESTEM SNR_{M1} drops to 60.6% in He, and to 42.0% in N₂ under the low beam current condition in this work. In the case of the He environment, as the ESTEM resolution hardly decreases up to 10 mbar, the degradation of the SNR_{M1} in He must be mainly caused by post specimen scattering of the image-forming electrons. That is to say, as the electrons carrying the sample information try to reach the ADF detector, they could be further scattered by the gas molecules in the post-sample gas pathway,^[5a] and are re-directed to a final scattering angle that is outside of the detector collection range, leading to a loss of signal from the solid sample. For the gases heavier than He, both pre-sample and post-sample gas scatterings may contribute to the degradation in ESTEM SNR_{sample}.

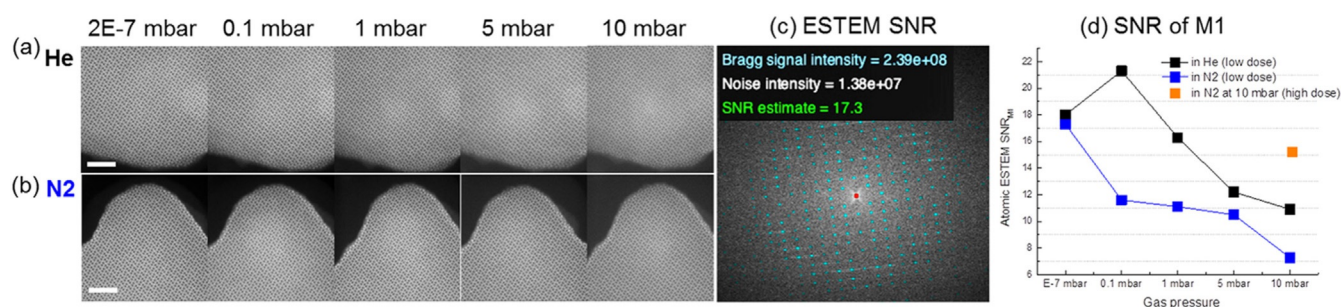


Figure 3. Experimental high-resolution ESTEM images of the M1 catalyst in [001] zone axis from high vacuum to 10 mbar in a) He and b) N₂. Scale bar is 10 nm. c) The quantification of atomic ESTEM image SNR of M1 by using the fast Fourier transform (FFT) measurement (for details see the Experimental Section). d) The FFT measured SNR of the M1 experimental ESTEM images in He and N₂ gas environments as a function of pressure.

Figure 4a,b present the approach and results of the ESTEM resolution evaluation over the M1 crystal in He and in N₂ up to 10 mbar. The large unit cell and thus densely packed diffraction spots of the M1 crystal in the [001] projection provide high sensitivity for resolution estimation. By measuring the ESTEM resolution on multiple M1 particles at different gas pressures (section 6 in the Supporting Information), we find that the He gas hardly affected the ESTEM resolution (resolution drop < 0.02 Å at 10 mbar) whereas the presence of N₂

leads to noticeable resolution degradation (> 0.40 Å at 10 mbar), under the low beam current imaging condition. To understand this difference in the ESTEM resolution dependence on the gas type, we studied the cause of STEM resolution degradation. It is known that the resolution of STEM is governed by the size of the converged probe.^[15] In conventional microscopes, the integrity of the STEM probe is preserved owing to the large electron mean free path under high vacuum; in the DP gas cell, prior to interacting with the sample, the STEM probe has to pass through the pre-sample gas species, which leads to extra scattering and possible diffusion of the originally sharp probe. If we assume that the gas species along the pre-sample pathway are acting collectively as a solid foil, the gas-induced STEM probe spreading can then be considered in a similar way to the beam broadening *b* caused by a (thick) sample. This probe broadening *b* can be estimated quantitatively based on Bothe's multiple-scattering theory,^[16]

$$b = 1.05 \times 10^3 \left(\frac{\rho}{W}\right)^{1/2} \frac{Z}{E} \frac{1 + E/E_0}{1 + E/2E_0} L^{3/2} \quad (1)$$

in which ρ , W , and Z are mass density, the mean molar mass, and the mean atomic number of a chosen solid, E is the microscope acceleration voltage in eV and E_0 is 1 eV. It shows that *b* increases with the 3/2 power of the sample thickness.

Considering that silicon nitride (Si₃N₄) is commonly used as the window material for the membrane windowed (MW) environmental gas cell, we chose it as the gas-equivalent solid foil. Based on the idea gas law, at a given pressure (P) and temperature (T), the reversed molar volume of a gas with a thickness of L_{gas} is equal to the reversed molar volume of Si₃N₄ with a thickness of L_{Si3N4} ,

$$\frac{P}{RT} L_{\text{gas}} = \frac{\rho}{W} L_{\text{Si3N4}} \quad (2)$$

in which R is the gas constant, W is 20.0 g mol⁻¹, and ρ is 3.2 × 10⁶ g m⁻³ for Si₃N₄. However, the above equation does not specify the type of the gas, that is, any 10 mbar gases at 300 K with a gas pathway of 2.7 mm are equivalent to 6.75 nm Si₃N₄. Clearly, this simple estimation is too generalized for any 10 mbar gases regardless of their type and thus cannot explain the difference in ESTEM resolution observed in He and in N₂. To take the nature of the gas into consideration, we revise the above equation by weighting both sides with the total scattering cross section σ and distinguishing gases by including the number of atoms in a gas molecule M ,

$$M \frac{P}{RT} L_{\text{gas}} \sigma_{\text{gas}} = \frac{\rho}{W} L_{\text{Si3N4}} \sigma_{\text{Si3N4}} \quad (3)$$

With this modification, the equivalent Si₃N₄ thicknesses of He and N₂ are 0.51 nm and 21.29 nm, respectively at 10 mbar (Table S2 in the Supporting Information). Thus, the theoretical probe broadening *b* as well as the corresponding ESTEM resolution reduction ΔR were estimated. The theoretically estimated ESTEM resolution drops are plotted as solid lines in Fig-

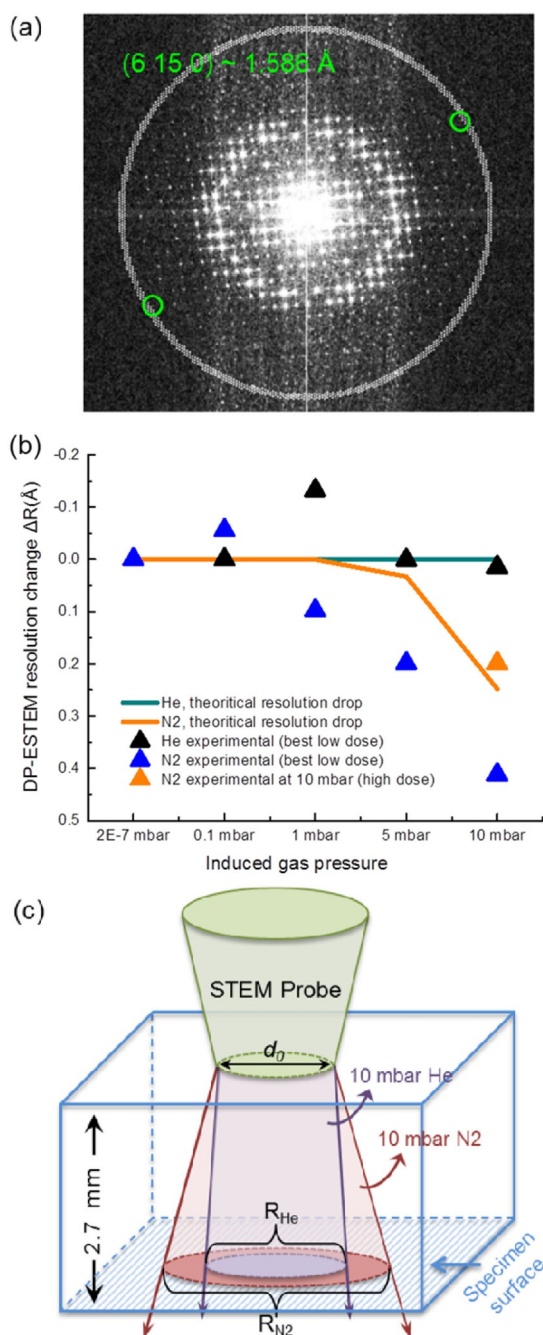


Figure 4. a) Experimental ESTEM resolution estimation based on the FFT of an atomic M1 image. b) Theoretical and experimental ESTEM resolution of M1 in He and N₂ up to 10 mbar. c) Schematic illustration of pre-sample gas introduced STEM probe spreading.

ure 4b). It shows that at 10 mbar, ESTEM resolution change is negligible in the He gas; whereas 2.7 mm N₂ leads to about 0.25 Å degradation in ESTEM resolution in theory. Notably the apparent probe broadening b should be added to the original probe size in quadrature to reflect the Gaussian-distribution nature of the STEM probe intensity.

Thus, as schematically illustrated in Figure 4c, after taking the gas type into account, the above theoretical estimation explains qualitatively the observed difference in the trend of the ESTEM resolution up to a higher pressure between the light and heavy gas environment. It is worth mentioning that the unpromising ESTEM resolution measured in N₂ (blue triangles in Figure 4b) was under the low beam current imaging condition used throughout this work. This low-dose resolution can be boosted by adjusting the STEM imaging conditions if the sample is not damaged and there are no kinetic changes in the reaction caused by the elevated current (details will be discussed in the next section).

Comments on electron dose and dose rate

To examine if the low beam current imaging conditions used in this work become limiting factors for ESTEM image quality and resolution with the presence of gas, we tested the above ESTEM SNRs, contrast, and resolution at different electron dose and dose rates, respectively, in 10 mbar N₂ environment. As shown in Figure 5, both of the SNRs of the amorphous carbon and of the M1 sample, and the ESTEM resolution increase along with the increase of total accumulated electron dose per image frame; whereas, such correlations are not observed on varying the dose rate (Figure S7 in the Supporting Information). In particular, for the atomically resolved ESTEM images of the M1 catalyst in 10 mbar N₂, by increasing the electron dose from the pre-set low dose ($8.24 \times 10^2 \text{ e} \text{ \AA}^{-2}$) to a relatively higher dose of $6.57 \times 10^3 \text{ e} \text{ \AA}^{-2}$, the SNR_{M1} is increases from 7.21 to 15.20 (the orange square in Figure 3d), and the resolution drop is mitigated to about 0.20 Å (Figure 4b), agreeing well with the theoretical resolution estimation. This suggests that both ESTEM SNR and resolution depend on the accumulated electron dose in an image, which is fundamentally different from the dose-rate dependence found for the ETEM resolution.^[11a,b] On the other hand, the ESTEM contrast of the amorphous carbon remains largely constant regardless of the electron dose and dose rate used for imaging (notably the fluctuations in contrast at extremely low dose/dose-rate are caused by the high uncertainties in determining the contrast). This suggests that the “Z-contrast” nature of the STEM imaging mode, and thus the elemental indications of the STEM intensity, is still valid for ESTEM imaging with the consideration for environmental contribution.

Unlike the convoluted relationship between the TEM beam and gas species,^[5] a relatively simple picture might be possible to elucidate the gas effects in the STEM imaging mode. One such attempt is schematically illustrated in Figure 6a. In the post-sample region at the bottom half of the gas-cell chamber, the STEM image-forming electrons carrying the information of the sample are generally inelastic in nature. The interactions

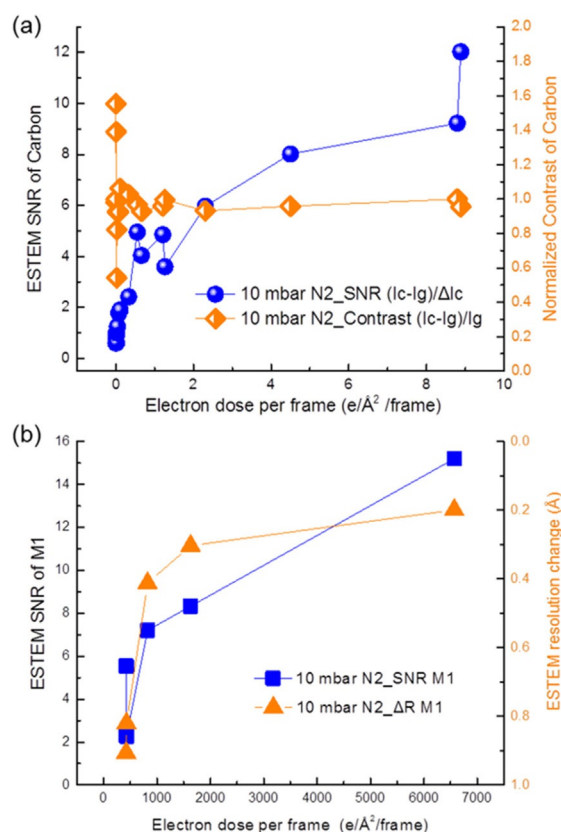


Figure 5. Experimentally measured electron dose dependent of a) the ESTEM SNR and contrast of carbon, and b) the SNR and ESTEM resolution (Figure S6 in the Supporting Information) over the M1 catalyst, in 10 mbar N₂.

between these electrons (i.e., sample signal) and the gas species (and/or bottom silicon nitride window) mainly lead to a diffusion of the STEM signal by scattering (some of) the image-forming electrons off the finite ADF detector. Thus, it results in losses in SNR and in resolution owing to the lack of signal. By increasing the electron dose through a longer dwell time, for example, the signal level can be retained and then recovers the ESTEM SNR and resolution. In other words, if a catalyst sample can tolerate an accumulated electron dose, the effects of gas species in the post-sample region can be largely alleviated. For example, excellent atomic ESTEM SNR was observed by using an electron dose of $10^4 \text{ e} \text{ \AA}^{-2}$.^[7b]

With the ESTEM signal diffusion retrieved by accumulating more electron doses, we can then propose the theoretically obtainable ESTEM image resolution for both DP-ESTEM and MW-ESTEM. Based on the multiple-scattering theory, in Figure 6b, the estimated resolutions for original STEM probe sizes of 0.78 Å (e.g., JEM-ARM 200F, probe-corrected), of 1.36 Å (e.g., Titan G² 300 kV), and of 1.90 Å (e.g., Tecnai G² F30 S-Twin) are plotted as a function of the thickness of the gas-equivalent silicon nitride (window). In general, the ESTEM probe broadening accelerates as the gas mass/pressure (or the pre-sample window thickness) becomes greater. For the DP gas cell (used in this work), the effect of 10 mbar N₂ on the ESTEM resolution is similar to the best obtainable resolution of a MW gas cell

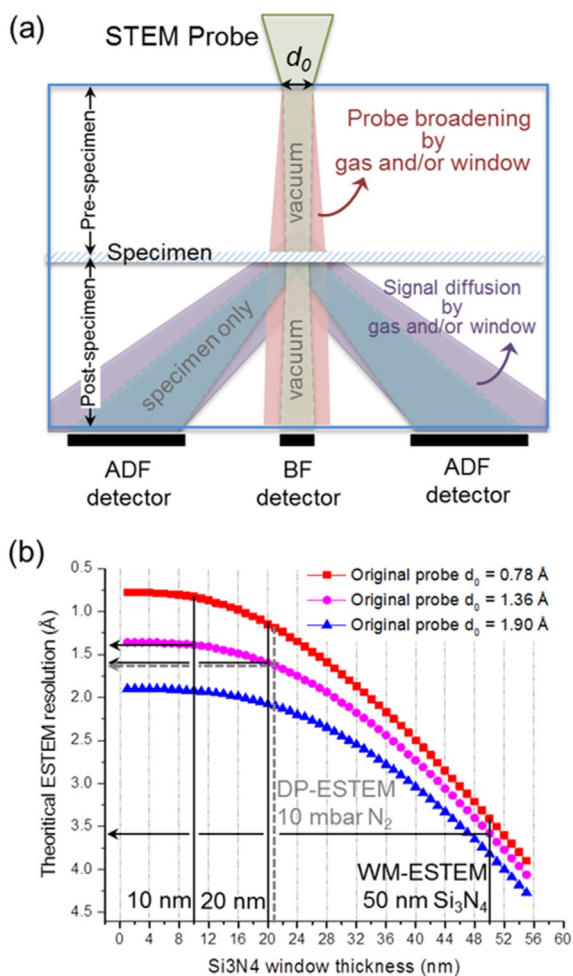


Figure 6. a) Schematic illustration of the pre- and post-sample gas effects on ESTEM probe and signal. b) Theoretical estimated ESTEM resolution as a function of silicon nitride thickness (Table S3 in the Supporting Information).

with a 20 nm-thick pre-sample Si₃N₄ window (if assuming the sample is attached to the top inside of the upper window). In a similar sense, the upper limit of 20 mbar N₂ in a DP gas cell (of 2.7 mm pre-sample gas pathway) is equivalent to a MW cell of an approximately 43 nm Si₃N₄ window (not shown here). On the other hand, as indicated by the comparison between a 10 nm and a 50 nm Si₃N₄ pre-sample window, the achievable ESTEM resolution for MW gas cells depends strongly on the window thickness (and for that matter, also the sample position). To eliminate the probe broadening effects, a Si₃N₄ window thinner than < 6 nm (or the N₂ in 2.7 mm gas-pathway is lower than approximately 3 mbar) is required. For a practical ESTEM probe of < 2.0 Å applicable for most metallic and metal oxide catalysts, an advanced objective lens is encouraged for DP-ESTEM and probe correction is required for MW-ESTEM.

Conclusions

Catalysis has benefited greatly from atomic-level imaging in modern (S)TEM, and in turn the kinetic nature of catalysis has also shaped the development of new capabilities in (S)TEM.

The recent advancements in situ environmental (S)TEM have further opened up unprecedented opportunities for obtaining experimental insights into the working structure of heterogeneous catalysts in technologically relevant environments. In addition, the presence of a catalytic environment such as pressurized gases poses new challenges to the (S)TEM sensitivity and resolvability and to our understanding of gas–electron interactions. In this work, we investigated both experimentally and theoretically the gas environment effects on image quality (in terms of sample contrast and SNR) and resolution in the directly interpretable ADF-STEM imaging mode in DP-ESTEM. The conclusions and guidelines identified are as follows:

i) The preconceived constrain imposed by the lower gas aperture in DP-ESTEM can be alleviated by loosening the inner ADF collection angle, without introducing image contrast reversals.

ii) The absence of the extra inelastic noise owing to the annular collection mode of the ADF-STEM imaging allows the ESTEM imaging mode to be free of intensity loss, and to maintain a good sensitivity in imaging the solid sample (sample SNR) with the presence of gases. Unlike the ETEM mode, ESTEM does not require a monochromator to achieve high quality imaging.

iii) The ESTEM sample contrast, owing to the incoherent nature of the ADF-STEM imaging mode, remains correlated to the (mean) atomic number of the solid sample with the consideration of the elastic contribution from the gas environment.

iv) The obtainable ESTEM resolution is determined mainly by the probe broadening effects induced by the pre-sample gas and electron beam interactions. Our theoretical estimation on the resolution shows that a probe-corrector is a necessity for high-resolution ESTEM imaging.

v) The practical ESTEM sample SNR and resolution are electron dose dependent, owing to the signal diffusion effect caused by the gas species in the post-sample region. In practice, the fact that the SNR and resolution both increase along with the accumulation of electron dose is beneficial for achieving high sensitivity and at the same time high-resolution ESTEM observations.

The ultimate challenge in imaging working catalysts in gas–solid heterogeneous catalysis is to be able to directly visualize the gas adsorbent at a catalyst surface with the reaction rate relevant high temporal resolution. Phase contrast in conventional HR-TEM has been used to image light materials (i.e., weak-phase objects) with the additional help of either phase plate^[17] or using off-axis holography.^[18] Although the frame time for one TEM image is relatively short compared with a typical STEM image, a HR-TEM focal-series is required for atomic interpretation, which takes a much longer time and then is low in temporal resolution. Recent developments in advanced STEM imaging have begun to leverage light-element imaging by, for example, ptychography,^[19] and to accelerate scanning speed without compromising image SNR by novel scan sampling.^[20] The combinations of these recent developments with the current high quality atomic ESTEM discussed in

this work, makes it a promising in situ tool-box for investigating catalytic dynamics.

Experimental Section

Sample preparation

Standard TEM lacey carbon Cu grids (Ted-Pella) were used as they were for ESTEM imaging of amorphous carbon. High purity crystalline MoVTeNb mixed oxide catalyst (M1 phase) was obtained by hydrothermal synthesis.^[9] TEM samples were prepared by crushing the M1 catalyst into a fine powder, and dry loading on an ultrathin carbon film on the lacey carbon support film Au grids (Ted-Pella). M1 samples were plasma cleaned 10 to 15 s prior to ESTEM imaging.

Environmental scanning transmission electron microscopy imaging

We employed a dedicated ETEM (FEI Titan 80/300) with differentially pumped gas cell system (objective lens pole pieces separation ~5.4 mm) housed in the EMSL user facility at PNNL. All ESTEM images shown in this work were acquired at 300 kV with a convergence semi-angle of 9.9 mrad without probe aberration correction. A low-angle annular dark field (LAADF) STEM mode with a collection range of 21–71 mrad (upper collection angle is limited by the DP gas cell aperture) was used throughout this work. A higher ADF detector inner semi-angle of 48 mrad (MAADF-STEM) was also tested with the presence of gases and details on the justification of using the LAADF-ESTEM imaging mode are given in section 2 in the Supporting Information. This microscope equipped with a field-emission gun produces a stable and bright electron probe. To determine the accurate electron current on the sample, we conducted a Faraday cup measurement by using an analytical holder (Gatan, Inc.) to calibrate the microscope screen dose-meter especially for the low current density region of <3 pA. To reproduce the low electron dose-rate and low accumulated dose imaging conditions that are often used for imaging delicate catalysts, a low beam current was kept around 1.5–3 pA and a short dwell time of 4 μ s/pixel was used for collecting all the ESTEM images (unless stated otherwise). The image magnification (and hence dose-rate) was chosen based on the size of the sample feature imaged. In particular, for the amorphous carbon, we used a magnification of $\times 115$ k corresponding to 3.34 \AA /pixel, dose rate 0.26 $\text{e}\text{\AA}^{-2}\text{s}^{-1}$ and dose per frame 4.50 $\text{e}\text{\AA}^{-2}$; the common magnification used for atomically resolved M1 catalyst is $\times 1800$ k corresponding to 0.22 \AA /pixel, dose rate $4.79 \times 10^1 \text{e}\text{\AA}^{-2}\text{s}^{-1}$, and dose per frame $8.24 \times 10^2 \text{e}\text{\AA}^{-2}$ (unless stated otherwise). The total dose was kept under the damage threshold for each M1 particle imaged.^[9]

Contamination from hydrocarbon build up in the ETEM column can impose difficulties during STEM imaging especially for a multi-user instrument. In this work, we found that the built-in plasma cleaner in the ETEM helped alleviate this issue. Prior to each ESTEM session, the plasma cleaning procedure was performed at 14 W (energy) for 10 h followed by 4 h purging with nitrogen. External plasma cleaning of the TEM sample is also encouraged to further eliminate contamination. During the ESTEM experiment, the back-pressure around the sample was pumped down to $< 2 \times 10^{-7}$ mbar after inserting the sample holder to set up a clean background. Ultra-pure He, H₂, N₂, and Ar was introduced around the sample to 0.1, 1, 5, and 10 ($\pm 5\%$) mbar, and flowed for about 10 min every time after reaching the targeting pressure before imaging. The op-

timal STEM imaging defocus was achieved by maximizing the contrast.

ESTEM image quantification

It is essential to read out the raw electron counts from an ESTEM image instead of the apparent image intensity, which varies depending on the brightness/contrast (B/C) setting. To avoid this, we used the original 16-bit.ser files or converting them to 16-bit (not 8-bit).tiff image files (so they can be read in DigitalMicrograph) for performing image intensity line profile. However, the ESTEM images shown in the figures in this paper were converted to 8-bit displays with a similar B/C setting to provide a reasonable demonstration of the gases effect.

For the ESTEM images of the gas background and amorphous carbon, as both are relatively uniform, applying the line profiling and extracting raw count intensity is straightforward (Figure 1). However, for the atomically resolved ESTEM images, line profile measurement could introduce ambiguity. For example, SNRs measured by line profiling are different depending on if it is along the slow or the fast scan direction.^[21] Here, we adopted a Matlab script using the fast Fourier transform (FFT) magnitudes measurement developed by Colin Ophus at Lawrence Berkeley National Laboratory. This script locates the Bragg peaks on the FFT pattern of an ESTEM lattice image. The sum of the Bragg peak intensities is the “useful signal” (amplitude squared), the sum of noise pixel intensities is the “noise”, and the ratio of the two gives the SNR. This method provides a relative SNR but the measurement is robust and highly reproducible. Notably to compare ESTEM images with different pixel sampling (thus different size of k frequency space in FFT), we defined a unified k frequency cutoff by applying a soft Gaussian low pass filters. By summing the signals and noise within the same size of k -space for different magnifications, we can then compare SNR across different reciprocal pixel size.

Acknowledgments

This research is part of the Chemical Imaging Initiative and a seed project conducted under the Laboratory Directed Research and Development Program at Pacific Northwest National Laboratory (PNNL). PNNL, a multiprogram national laboratory, is operated by Battelle for the Department of Energy under Contract DE-AC05-76RLO1830. A portion of the research was performed using the Environmental Molecular Sciences Laboratory (EMSL), a national scientific user facility sponsored by the Department of Energy's Office of Biological and Environmental Research and located at Pacific Northwest National Laboratory. Special thanks to Dr. Colin Ophus at Molecular Foundry, LBNL, for his generous help and providing the FFT magnitude Matlab script. The authors thank Dr. Libor Kovarik (EMSL, PNNL) for technical support on the ESTEM, and we also thank Daniel Melzer and Dr. Maricruz Sanchez-Sanchez at the Technical University of Munich for providing the M1 catalysts.

Conflict of interest

The authors declare no conflict of interest.

Keywords: environmental scanning transmission electron microscopy · gas atmosphere · gas–solid reaction · image resolution · sample signal to noise ratio

- [1] a) J. M. Thomas, P. A. Midgley, *ChemCatChem* **2010**, *2*, 783–798; b) R. Sharma, *Micron* **2012**, *43*, 1147–1155; c) P. A. Crozier, T. W. Hansen, *MRS Bull.* **2015**, *40*, 38–45; d) E. D. Boyes, P. L. Gai, *MRS Bull.* **2015**, *40*, 600–605; e) S. Helveg, C. F. Kisielowski, J. R. Jinschek, P. Specht, G. Yuan, H. Frei, *Micron* **2015**, *68*, 176–185.
- [2] L. Marton, *Bull. Acad. R. Belg. Cl. Sci.* **1935**, *21*, 553–560.
- [3] a) H. G. Heide, *J. Cell Biol.* **1962**, *13*, 147–152; b) E. J. Gallegos, *Rev. Sci. Instrum.* **1964**, *35*, 1123; c) H. Hashimoto, T. Naiki, *Jpn. J. Appl. Phys.* **1968**, *7*, 946; d) P. R. Swann, *High Voltage Microscope Studies of Environmental Reactions*, Univ. Calif. **1972**, pp. 878–904; e) H. M. Flower, *J. Microsc.* **1973**, *97*, 171–190; f) N. M. Rodriguez, S. G. Oh, W. B. Downs, P. Pattabiraman, R. T. K. Baker, *Rev. Sci. Instrum.* **1990**, *61*, 1863–1868; g) R. Sharma, K. Weiss, M. McKelvy, W. Glaunsinger, in *Fifty-Second Annual Meeting—Microscopy Society of America/Twenty-Ninth Annual Meeting—Microbeam Analysis Society, Proceedings* (Eds.: G. W. Bailey, A. J. GarrattReed), **1994**, pp. 494–495; h) E. D. Boyes, P. L. Gai, *Ultramicroscopy* **1997**, *67*, 219–232.
- [4] a) H. Yoshida, S. Takeda, *Phys. Rev. B* **2005**, *72*, 195428; b) J. F. Creemer, S. Helveg, G. H. Hoveling, S. Ullmann, A. M. Molenbroek, P. M. Sarro, H. W. Zandbergen, *Ultramicroscopy* **2008**, *108*, 993–998; c) P. L. Gai, E. D. Boyes, *Microsc. Res. Tech.* **2009**, *72*, 153–164; d) T. W. Hansen, J. B. Wagner, R. E. Dunin-Borkowski, *Mater. Sci. Technol.* **2010**, *26*, 1338–1344.
- [5] a) M. Suzuki, T. Yaguchi, X. F. Zhang, *Microscopy* **2013**, *62*, 437–450; b) J. B. Wagner, M. Belaggia, in *Controlled Atmosphere Transmission Electron Microscopy: Principles and Practice* (Eds.: T. W. Hansen, J. B. Wagner), Springer International Publishing, Cham, Switzerland, **2016**.
- [6] a) P. L. Hansen, J. B. Wagner, S. Helveg, J. R. Rostrup-Nielsen, B. S. Clausen, H. Topsoe, *Science* **2002**, *295*, 2053–2055; b) H. Yoshida, Y. Kuwachi, J. R. Jinschek, K. J. Sun, S. Tanaka, M. Kohyama, S. Shimada, M. Haruta, S. Takeda, *Science* **2012**, *335*, 317–319.
- [7] a) P. Li, J. Liu, N. Nag, P. A. Crozier, *Appl. Catal. A* **2006**, *307*, 212–221; b) S. Zhang, P. N. Plessow, J. J. Willis, S. Dai, M. J. Xu, G. W. Graham, M. Cargnello, F. Abild-Pedersen, X. Q. Pan, *Nano Lett.* **2016**, *16*, 4528–4534.
- [8] P. L. Gai, L. Lari, M. R. Ward, E. D. Boyes, *Chem. Phys. Lett.* **2014**, *592*, 355–359.
- [9] Y. Zhu, P. V. Sushko, E. Jensen, L. Kovarik, D. Melzer, C. Ophus, M. Sanchez-Sanchez, J. Lercher, N. Browning, **2017**, unpublished results.
- [10] P. A. Crozier, in *Scanning Transmission Electron Microscopy* (Eds.: S. J. Pennycook, P. D. Nellist), Springer, New York, **2011**, pp. 537–582.
- [11] a) J. R. Jinschek, S. Helveg, *Micron* **2012**, *43*, 1156–1168; b) A. N. Bright, K. Yoshida, N. Tanaka, *Ultramicroscopy* **2013**, *124*, 46–51; c) H. L. Xin, K. Niu, D. H. Alesm, H. Zheng, *Microsc. Microanal.* **2013**, *19*, 1558–1568; d) M. Ek, S. P. F. Jespersen, C. D. Damsgaard, S. Helveg, *Adv. Struct. Chem. Imaging* **2016**, *2*, 4.
- [12] a) M. M. J. Treacy, *J. Microsc. Spectrosc.* **1982**, *7*, 511–523; b) Z. W. Wang, Z. Y. Li, S. J. Park, A. Abdela, D. Tang, R. E. Palmer, *Phys. Rev. B* **2011**, *84*, 073408.
- [13] A. Rose, in *Advances in Electronics and Electron Physics, Vol. 1* (Ed.: L. Marton), Academic Press, San Diego, CA, **1948**, pp. 131–166.
- [14] V. Ortalan, A. Uzun, B. C. Gates, N. D. Browning, *Nat. Nanotechnol.* **2010**, *5*, 843–847.
- [15] N. D. Browning, M. F. Chisholm, S. J. Pennycook, *Nature* **1993**, *366*, 143–146.
- [16] L. Reimer, *Transmission Electron Microscopy*, Springer, Heidelberg, **1984**.
- [17] R. Danev, H. Okawara, N. Usuda, K. Kametani, K. Nagayama, *J. Biol. Phys.* **2002**, *28*, 627–635.
- [18] M. Linck, B. Freitag, S. Kujawa, M. Lehmann, T. Niermann, *Ultramicroscopy* **2012**, *116*, 13–23.
- [19] H. Yang, R. N. Rutte, L. Jones, M. Simson, R. Sagawa, H. Ryll, M. Huth, T. J. Pennycook, M. L. H. Green, H. Soltau, Y. Kondo, B. G. Davis, P. D. Nellist, *Nat. Commun.* **2016**, *7*, 12532.
- [20] a) L. Kovarik, A. Stevens, A. Liyu, N. D. Browning, *Appl. Phys. Lett.* **2016**, *109*, 164102; b) T. Dahmen, M. Engstler, C. Pauly, P. Trampert, N. de Jonge, F. Mücklich, P. Slusallek, *Sci. Rep.* **2016**, *6*, 25350.
- [21] Y. Zhu, C. Ophus, J. Ciston, H. Wang, *Acta Mater.* **2013**, *61*, 5646–5663.

Manuscript received: March 16, 2017

Revised manuscript received: May 21, 2017

Accepted manuscript online: May 24, 2017

Version of record online: August 2, 2017